Journal of Petroleum Science and Engineering 200 (2021) 108230

Contents lists available at ScienceDirect

Journal of Petroleum Science and Engineering

journal homepage: http://www.elsevier.com/locate/petrol

Understanding pore evolution in a lacustrine calcareous shale reservoir in the oil window by pyrolyzing artificial samples in a semi-closed system

Taoli Wang [a,b], Qingtao Wang [c,*], Hong Lu [a,**], Ping'an Peng [a], Xin Zhan [d]

[a] State Key Laboratory of Organic Geochemistry, Guangzhou Institute of Geochemistry, Chinese Academy of Sciences, Guangzhou, 510640, China
[b] University of Chinese Academy of Sciences, Beijing, 100049, China
[c] State Key Laboratory of Continental Dynamics, Department of Geology, Northwest University, Xi'an, 710069, China
[d] Geology and Geophysics Program, Missouri University of Science and Technology, Rolla, MO, 65409, USA

ARTICLE INFO

Keywords:
Lacustrine calcareous shale
Shale oil
Pore evolution
Dissolution pores
Oil saturation
Lucaogou Formation

ABSTRACT

Calcareous shale is a favorable target for shale oil exploration, because shale oil moves more easily in calcareous shale than in clay-rich shale and the high carbonate content is beneficial to shale fracturing. Although shale oil exploration has been undertaken successfully in marine carbonate-rich shale (e.g., the Eagle Ford shale) in the USA, no major breakthrough has yet been made considering lacustrine calcareous shale. The lack of understanding pore evolution in lacustrine calcareous shale increases exploration risk. Thus, an integrated analysis (Rock-Eval pyrolysis, X-ray diffraction (XRD[1]), low-pressure gas adsorption, field emission scanning electron microscopy (FE-SEM[2]), energy dispersive X-ray spectroscopy (EDS[3]), and helium pycnometry) of lacustrine calcareous shale from the Lucaogou Formation in the Santanghu Basin and of pyrolyzed shale was undertaken to document the hydrocarbon generation and expulsion, oil bearing capacity, and evolution of pores in the oil window. The thermal stress was calculated as the vitrinite reflectance equivalent (%Re[4]) based on the Easy%Ro method. The experimental results showed that the residual oil content and oil saturation index (OSI[5]) increased with increasing maturity at 0.6–1.29 %Re. The clogging of pores by generated oil and intense compaction caused a decrease in the volume of mesopores and macropores at 0.79–1.2 %Re, while abundant organic matter (OM[6]) pores formed due to hydrocarbon generation and expulsion at 1.29 %Re. Micron-scale dissolution pores and shrinkage OM pores contributed considerably to the total porosity, which improved the performance of the lacustrine calcareous shale reservoir at 1.0–1.29 %Re. Accordingly, the maturity range of 1.2–1.29 %Re is favorable for shale oil exploration in lacustrine calcareous shale due to the high OSI and the widely developed dissolution pores and shrinkage OM pores.

Credit author statement

Taoli Wang, Investigation, Data curation, Writing – original draft. Qingtao Wang, Conceptualization, Methodology, Writing – review & editing. Hong Lu, Resources, Funding acquisition. Ping'an Peng, Supervision. Xin Zhan, Writing – review & editing

1. Introduction

Shale oil exploration and shale oil reservoir evaluation have drawn considerable attention in recent years (Zhang et al., 2014; Wang et al., 2015a), as increased shale oil production could reduce the disparity between global fossil energy supply and demand. Shale oil is a liquid hydrocarbon, significant in terms of exploration, which is stored in effective source rocks in a free phase (condensate oil), adsorbed phase, and dissolved phase (dissolved in natural gas, kerogen, and residual water) (Jarvie, 2012; Zhang et al., 2012). Shale oil in North America is mainly contained in marine strata, while the majority of shale oil in China is stored in lacustrine strata (Zou et al., 2013; Wang et al., 2015a). In China, the lacustrine strata are widely distributed and have a large variation in total organic carbon (TOC[7]) content and lithology, including organic-rich mudstones interbedded with sandstone, sandy mudstone, and carbonate rocks (Du et al., 2014; Wang et al., 2015b). For example, the Triassic formation in the Ordos Basin, the Cretaceous formation in the Songliao Basin, the Permian formation in the Junggar

* Corresponding author.
** Corresponding author.
E-mail address: wqtok2005@163.com (Q. Wang).

https://doi.org/10.1016/j.petrol.2020.108230
Received 15 November 2019; Received in revised form 30 November 2020; Accepted 2 December 2020
Available online 15 December 2020

Abbreviations

X-ray diffraction (XRD)
Field emission-scanning electron microscopy (FE-SEM)
Energy dispersive X-ray spectroscopy (EDS)
Vitrinite reflectance equivalent (%Re)
Oil saturation index (OSI)
Organic matter (OM)
Total organic carbon (TOC)
Intra-particle (intraP)
Vitrinite reflectance (Ro)
Free hydrocarbons (S_1)
Oil potential (S_2)
Peak temperature of S_2 (T_{max})
Hydrogen index (HI)
Density functional theoretical model (DFT)
Pore size distribution (PSD)
Secondary electron (SE)
International Union of Pure and Applied Chemistry (IUPAC)
Inter-particle (interP)

and Santanghu Basins, and the Paleogene formation in the Bohai Bay Basin are prospective exploration zones for shale oil or tight oil (Yang et al., 2020).

The pore composition of shale determines its storage capacity and ability to transmit shale oil during exploration (Ross and Bustin, 2007; Chalmers et al., 2012). Consequently, an estimation of pore development in shale is of great significance, which helps guide shale oil exploration. Shale has significant heterogeneity in different geological conditions; hence, pore evolution in shale is a complex geological process that is restricted by its own physical and chemical properties and diagenesis. Numerous studies have been conducted to study the factors influencing the development and evolution of organic matter (OM) pores and mineral pores in shale (Loucks et al., 2009, 2012; Curtis et al., 2012; Pommer and Milliken, 2015; Mathia et al., 2016). OM pores were present during maceral deposition, and were possibly influenced by the OM type and original molecular structure within the macerals (Curtis et al., 2012; Fishman et al., 2012; Löhr et al., 2015); nevertheless, maturity has been considered as the primary factor, at least to a large extent, which controls the development of OM pores (Loucks et al., 2009; Chen and Xiao, 2014). Mineral pores could have formed due to the compressional contact between mineral grains and by the mechanical rearrangement of phyllosilicate platelets during diagenesis (Fishman et al., 2012; Loucks et al., 2012). Furthermore, clay mineral intra-particle (intraP[8]) pores occurred within loosely aggregated clay platelets, while numerous OM pores were observed in an organo-clay complex (Wang et al., 2018). However, the mineral pores might have largely decreased due to strong mechanical compaction and cementation, resulting in low pore connectivity (Loucks et al., 2012; Li et al., 2018). Thus, dissolution pores with a relatively large pore volume are critical toward improving the storage capacity of shale (Luan et al., 2016; Nie et al., 2019).

Dissolution pores develop through dissolution of chemically unstable minerals during diagenesis (Loucks et al., 2012; Milliken et al., 2013). Lacustrine calcareous shale contains more carbonate minerals than mudstone and siliceous shale; hence, dissolution pores develop expectedly in lacustrine calcareous shale. Organic acids are considered to have high dissolution capacity, and which could be produced by the thermal degradation of kerogen with a vitrinite reflectance (Ro[9]) of 0.89–1.25% (Seewald, 2003; Li et al., 2018). Hence, the storage capacity for shale oil determined by the pore network in lacustrine calcareous shale is dynamic, considering increasing thermal stress. Shale oil accumulation is strongly associated with hydrocarbon generation and expulsion in the oil window. Hydrocarbon mobility is significantly higher in calcareous shale than in mudstone shale (Li et al., 2016) due to its weak oil wettability; moreover, the high carbonate content makes calcareous shale sensitive to fracturing. The combined effects of the above two make calcareous shale a favorable lithofacies for shale oil exploration (Liu et al., 2015; Wang and Wang, 2020). However, few studies have considered the pore characteristics of lacustrine calcareous shale in comparison to that of mudstone and siliceous shale (Ehrenberg and Nadeau, 2005; Chalmers et al., 2012; Clarkson et al., 2012; Mathia et al., 2016).

The Lucaogou Formation in Santanghu Basin mainly contains calcareous mudstone and dolomitic mudstone with a maximum accumulated thickness of 800 m (Huang et al., 2012; Liang et al., 2012; Liu et al., 2012a). The test oil production of a single well in Malang Sag was 22 m^3/day, demonstrating the significant potential for shale oil exploration (Liang et al., 2012). Here, typical lacustrine calcareous shale collected from the middle Permian Lucaogou Formation in the Santanghu Basin, Northwest China, was chosen to be pyrolyzed in a semi-closed system, to illustrate the oil bearing capacity and pore evolution characteristics of lacustrine calcareous shale in the oil window. Moreover, the variation of expelled and residual hydrocarbons and their influence on the pore evolution of lacustrine calcareous shale during organic matter maturation is also discussed, which could provide insights into the mechanism for storing shale oil in lacustrine calcareous shale.

2. Geological setting

The Santanghu Basin bound by Mongolia to the northeast, the Turpan-Hami Basin to the south, and the Junggar Basin to the west, is one of the basins with the most potential for shale oil development within the Xinjiang Uygur Autonomous Region, Northwest China. The basin is a long strip trending northwest-southeast, covering an area of $\sim 2.3 \times 10^4$ km^2 (Fig. 1), and is a superimposed basin, sandwiched between the Tianshan and Altai Mountains (Ma et al., 2019). The basin has experienced two important stages of tectonic evolution: basement formation during the Paleozoic and the evolution of an intra-continental foreland basin since the Permian period. During the early-middle Permian period, the basin transformed into intra-continental rifting and drifting due the regional crustal extension (Liu et al., 2012b). From the late Permian to the early Triassic, the basin underwent regional compression. The first-order and second-order structural units eventually formed due to strong tectonic activity during the late Cretaceous to the Paleogene and Quaternary (Liu et al., 2019b). The first-order structural units comprise the northeast fold-thrust belt, the central depression belt, and the southwestern fold-thrust belt from the northeast to southwest. The second-order structural units comprise four uplifts (Shitoumei, Chahaquan, Fangfangliang, and Weibei uplifts) and five sags (Hanshuiquan, Tiaohu, Malang, Naomaohu, and Suluke sags), which are all contained in the central depression (Fig. 1).

The Lucaogou Formation is a potential exploration target for tight oil (including shale oil) and is the source rock for tight oil in the overlying Tiaohu Formation in the Santanghu Basin due to its favorable thickness and organic-richness (Li et al., 2015b; Zhang et al., 2018). The Lucaogou Formation, which is widespread in the Malang and Tiaohu sags, is a lacustrine system with mixed carbonate-siliciclastic sediments, including carbonate shale, siliceous shale, calcareous mudstones, dolomitic mudstones, and other fine-grained sediments (Liu et al., 2017; Zhang et al., 2018). The organic-rich (TOC of 2.8–11.4%) carbonate-dominated mudrocks of the Lucaogou Formation from the lower to the upper section deposited in a lake evolved from an under-filled stratified evaporative (saline) setting to a more balanced-filled lake basin with higher water input. The organic matter was dominated by Type I with a vitrinite reflectance of 0.47–0.58%, indicating that the Lucaogou Formation was in the early oil window (Hackley et al., 2016). The lacustrine calcareous shale was collected from the Yuejingou section located in the southwestern edge of the

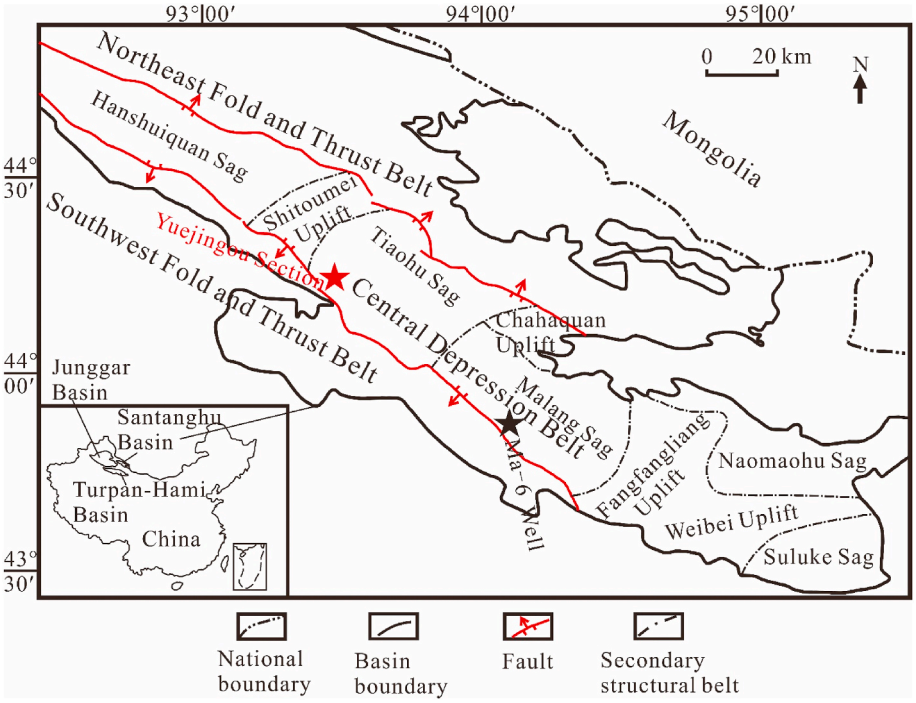

Fig. 1. Distribution of structural units in the Santanghu Basin and location of the samples collection (Modified from Ma et al., 2019).

Santanghu Basin (Fig. 1). The thickness of the Lucaogou Formation in this section was 222 m (Liu et al., 2012b). The calcareous mudstone and dolomitic mudstone in the Lucaogou Formation hold significant shale oil potential due to their favorable mineral composition (Liu et al., 2017; Zhang et al., 2018).

3. Material and methods

3.1. Sample and optimization methods

Prior to this study, Rock-Eval analysis and X-ray diffraction (XRD) were conducted for three outcrop samples collected from the Yuejingou section and for two core samples collected from the Ma-6 and Ma-10 Wells in Malang Sag to obtain their organic geochemical and mineral compositions. The Rock-Eval 6 pyrolysis analyzer was used to measure the free hydrocarbons (S_1^{10}), oil potential (S_2^{11}), peak temperature of S_2 (T_{max}^{12}), and hydrogen index (HI^{13}) (Fishman et al., 2012; Ma et al., 2019). S_1 represents the thermally released hydrocarbons before 300 °C, while S_2 represents the hydrocarbons released during 300–650 °C. T_{max} is generally used as an indicator of the thermal maturity of organic matter. HI is defined as the value of S_2 normalized by TOC. Pulverized samples of particle-size <0.074 mm (200 mesh) were analyzed by the Olympus BTX-II X-ray diffractometer equipped with a Co X-ray source operated at 31 kV and 0.4 mA. The whole-bulk minerals were analyzed by stepwise scanning measurements performed between 3° and 55° (2θ), using a 0.02° (2θ) scanning-interval. The exposure time was 70 min, while the exposure rate was thrice per minute (Zheng et al., 2018). The organic geochemical parameters and mineral compositions of the five samples are shown in Table 1 and Table 2, respectively.

The samples studied here were selected among the five samples considering that they were characterized by low maturity, high TOC, and high carbonate content. Samples with low maturity and high TOC were suitable for simulation experiments, while the high carbonate content is beneficial for observations on dissolution pores. Moreover, a large amount of samples was necessary because at least six cylindrical samples were used in the pyrolysis experiment. The core samples were insufficient for preparing the plug samples. Ultimately, a calcareous shale (YJG-OR) was selected, which was an outcrop sample collected from the Yuejingou section of the middle Permian Lucaogou Formation. A low maturity (0.52 %Ro) was reported by Du et al. (2014), and was indicated by a low T_{max} value (436 °C), while a dominant presence of Type I organic matter was suggested by a high HI and low T_{max} value (Table 1). This sample collected from the Yuejingou profile had high carbonate content (24.2% dolomite and 5.4% calcite) and high albite content (29.8%) (Table 2), which corresponded with that of the main lithofacies reported in the Lucaogou Formation (Liu et al., 2017; Zhang et al., 2018).

Table 1
Basic organic geochemical parameters of samples collected from the Yuejingou profile, Well Ma-6, and Well Ma-10.

Sample	Depth (m)	S_1 (mg/g)	S_2 (mg/g)	T_{max} (°C)	HI (mg/g TOC)	TOC (%)
YJG-OR	Outcrop	1.0	114.0	436.0	655.8	18.5
YJG-2	Outcrop	0.4	62.0	433.0	552.0	11.2
YJG-10	Outcrop	2.3	119.8	435.0	682.0	17.6
Ma-6	3130.3	0.3	24.1	441.0	661.0	3.7
Ma-10	2295.5	0.8	81.9	446.0	848.0	9.7

3.2. Experimental procedure

Here, a semi-closed thermal simulation of hydrocarbon generation device was used to pyrolyze the lacustrine calcareous shale within the oil window (Fig. 2) (Fu et al., 1990). Artificially matured samples with different maturities could be obtained, while hydrocarbon products could be collected timely through this device. A fresh and cleaned cylindrical sample of the calcareous shale (approximately 2.1 cm diameter and 3.0 cm height) was obtained by drilling using a small cylinder. A stainless-steel cylinder and other parts were carefully cleaned and heated at 450 °C for an hour to remove any residual organic material before placing them into the oven.

First, the small cylindrical calcareous shale sample was loaded into the stainless-steel cylinder fixed with a red copper-ring and bottom pressure-cap; quartz sand was filled around this sample. Then, the loose

Table 2
Mineral composition of samples collected from the Yuejingou profile, Well Ma-6, and Well Ma-10.

Sample	Quartz (%)	Albite (%)	Dolomite (%)	Calcite (%)	Gypsum (%)	Chlorite (%)	Pyrite (%)	Illite (%)
YJG-OR	16.9	29.8	24.2	5.4	11.0	12.6	n.d.	n.d.
YJG-2	30.3	29.9	10.8	4.1	12.7	12.1	n.d.	n.d.
YJG-10	17.4	24.8	27.8	7.7	10.7	11.7	n.d.	n.d.
Ma-6	25.1	16.5	8.9	24.7	n.d.	n.d.	12.5	12.3
Ma-10	43.3	23.3	7.0	7.5	n.d.	n.d.	9.7	9.2

n.d.: not detected.

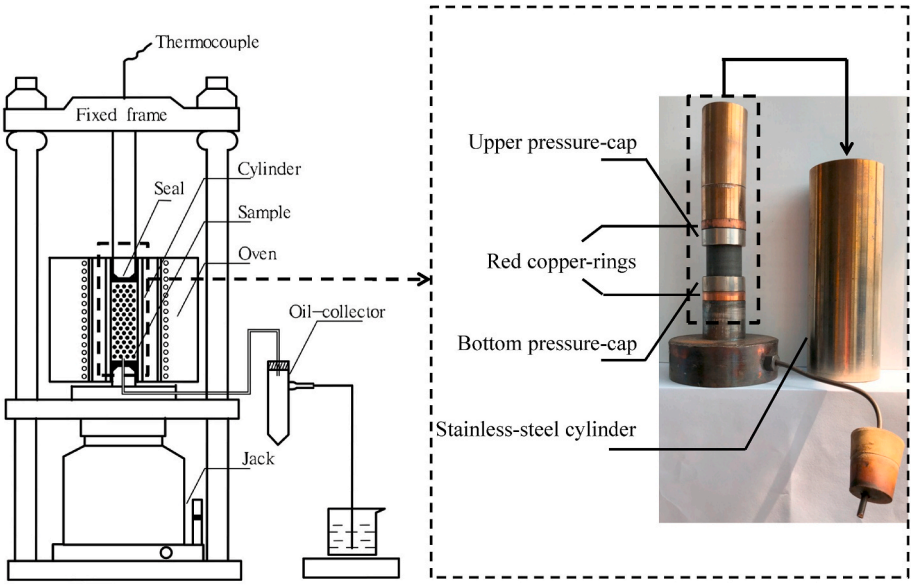

Fig. 2. Schematic diagram of the semi-closed thermal simulation of hydrocarbon generation device (after Fu et al., 1990).

quartz sand was compacted and the top of the stainless-steel cylinder was sealed with another red copper-ring and an upper pressure-cap under a vertical pressure of 63 MPa. The heating oven was sheathed on the exterior of the stainless-steel cylinder and connected with a thermocouple. During the pyrolysis experiment, artificially matured samples with a specific maturity attained thermal stress levels of 0.6–1.29 %Re (vitrinite reflectance equivalent based on the Easy%Ro method; Sweeney and Burnham, 1990) across the oil generative window. The oven was programmed to temperatures of 25–360 °C for an hour and then held for 0.2, 3.8, and 21 h to attain samples with %Re values 0.6, 0.79, and 1.0, respectively. Then, the oven was programmed from 360 °C to 370 °C for 0.5 h, and then held for 26.5 h and 51.5 h to attain samples with %Re values of 1.2 and 1.29, respectively. The above five samples with specific maturities were attained through five independent experiments. The vertical pressure was maintained at 63 MPa throughout the experiment. The total liquid hydrocarbon collected from the oil-collector and washed from the inner-wall of the stainless-steel cylinder and the pipe was recorded as the expelled oil. A small block of each pyrolyzed sample was ground into grains of size greater than a 120 mesh, and Soxhlet extracted by mixing a solution of dichloromethane and methanol (v:v = 9:1) over 72 h to obtain chloroform bitumen "A" (residual oil).

3.3. Low-pressure CO_2 and N_2 isothermal adsorption

Low-pressure gas isothermal adsorption is an effective method widely used to quantitatively study shale pore structure (Ross and Bustin, 2009; Tian et al., 2013). Carbon dioxide adsorption helps test micropores (<2 nm), while nitrogen adsorption helps characterize mesopores and macropores (>2 nm) (Wang et al., 2018). Low-pressure gas adsorption isotherms were obtained using the Micromeritics ASAP-2460 Accelerated Surface Area and Porosimetry System. Extracted samples were obtained through Soxhlet extraction. A part of each sample was crushed to 60–120 mesh (0.250–0.125 mm), as recommended by Wei et al. (2016a), and dried in a vacuum chamber at 60 °C for over 12 h to remove residual volatiles and free water before analysis. CO_2 isothermal adsorption was conducted at 273.15 K with a relative pressure (p/p_0) ranging from 0.000 06 to 0.03. N_2 isothermal adsorption was performed at 77 K with a relative pressure ranging from 0.005 to 0.998. The density functional theoretical model (DFT[14]) was used to characterize the pore volume and specific surface area of all nanopores. The pore size distribution (PSD[15]) of the investigated samples were obtained using the DFT model based on a combination of the N_2 and CO_2 adsorption isotherms (Wang et al., 2018). It is challenging to select an accurate simplex pore shape model to obtain the pore structures, as pores vary widely by size, type, and morphology in shale (Wei et al., 2016b). However, the DFT model was developed based on slit-like pores in activated carbon (Dombrowski et al., 2000), which is considered to help accurately evaluate pore-size distributions. This model is popularly used to obtain pore structure data of porous media (e.g., carbon black or shale) (Dombrowski et al., 2000; Wang et al., 2019), because organic carbon and slit-like pores are present in shale. Slit-like pores are strip-shaped, which is one of typical types of pores in shale.

3.4. Field emission scanning electron microscopy (FE-SEM) and energy dispersive X-ray spectroscopy (EDS)

Untreated and pyrolyzed samples of the lacustrine calcareous shale were cut into small cubes (1.0 cm × 0.5 cm × 0.5 cm), which were then polished by 300, 800, 1500, and 3000 mesh sandpaper in turn. Thereafter, the plane perpendicular to the bedding on each cube was polished by an Ar-ion milling-instrument (IM4000, Hitachi High-Tech) with an

acceleration voltage of 3 kV and a milling-time of 4–8 h to produce a glazed surface with minor surficial variation. A Hitachi S8010 system with an acceleration voltage of 1.5 kV was used to obtain secondary electron (SE^{16}) images; the working distance ranged between 2.5 mm and 8 mm. The FE-SEM is a qualitative technique to understand the size, type, location, and arrangement of pores in shale (Loucks et al., 2012). The elemental composition was obtained through a Hitachi S8010 system associated with an EDS microprobe. An acceleration voltage of 15 kV and a resolution ratio of 130.2 eV were used during the EDS.

3.5. Total porosity measurement

The total porosity can be determined by the difference between the grain density and bulk density (Chalmers et al., 2012; Tian et al., 2013). The small cylindrical shale blocks (described in section 3.2) were used to determine the grain density by helium pycnometry at a pressure of less than 25 psia following overnight drying at 110 °C in a vacuum oven. To measure the bulk density, the shale blocks were weighed in air before and after coating with paraffin of known density (ρ = 0.9 cm^3/g); thereafter, the paraffin-coated samples were weighed both in air and water at room temperature (~25 °C). Thus, the volume of the shale blocks could be determined by the difference between the total volume (of shale and paraffin) and the volume of the paraffin. Subsequently, the bulk density was calculated by considering the weight in air and volume of the shale blocks, as described by Tian et al. (2013). Thereafter, the total porosity was calculated by the following equation:

$$\Phi = 100 \times \left(1 - \frac{\rho_{bulk}}{\rho_{grain}}\right) \quad (1)$$

where, Φ is the total porosity (%); ρ_{bulk} and ρ_{grain} are the bulk density (cm^3/g) and grain density (cm^3/g), respectively.

4. Results

4.1. Evolution characteristics of organic geochemical parameters

TOC values of the investigated samples obtained through the Rock-Eval analysis first showed an increase (from the original 18.5%–21.4%) and then a decrease (to 11.7%) with increasing maturity (Fig. 3a). The initial increase could be attributed to a reduction in the shale mass caused by the decomposition/dehydration of minerals, while the decrease in TOC at high temperatures mainly occurred due to hydrocarbon generation. The decrease in TOC corresponded to the sharp decrease in the HI at a maturity of >1.0 %Re (Fig. 3b). The TOC values kept dropping (0.79–1.29 %Re), indicating a continuous thermal degradation of kerogen to hydrocarbons. Part of the generated oil was expelled, while part remained in the source rocks; this differed from the thermal decomposition of bitumen into oil, considering the Woodford Shale and Phosphoria Retort Shale, at approximately 0.6–1.3 %Ro and 0.4–1.3 %Ro, respectively (Lewan, 1985). The cumulative amount of expelled oil continuously increased from the initial 21.2 mg/g rock to the final value of 208.9 mg/g rock. However, the amount of expelled oil, considering the same maturity gradient, exhibited a stepwise change, varying from 21.2 mg/g rock to 63.4 mg/g rock (Fig. 3c). The amount of expelled oil at 1.29 %Re was lower than that at 1.2 %Re, implying that the cracking of oil to gas began at 1.29 %Re. Here, the yield of the expelled and residual oil was significantly less than that obtained through the hydrous pyrolysis of the Woodford Shale and Phosphoria Retort Shale. This occurred because the water dissolved in the bitumen acted as a source of hydrogen to promote thermal cracking over cross-linking, enabling higher liquid hydrocarbon yields (Lewan and Roy, 2011). The amount of residual oil (chloroform bitumen "A") continuously increased with increasing thermal stress (Fig. 3e). S_1 represents the amount of free oil in the shale obtained through thermal evaporation; moreover, the variation of (S_1 × 100)/TOC was similar to that of residual oil/TOC (Fig. 3d, f).

4.2. Characteristics of N_2 and CO_2 adsorption isotherms

Fig. 4 shows the low-pressure CO_2 adsorption isotherms for the investigated samples before and after solvent extraction (denoted as unextracted and extracted samples, respectively); the isotherms conformed to the Type I(b) adsorption isotherm (Figs. 4 and 5a), suggesting that micro-porous solids having relatively small external surfaces contained in samples (Thommes et al., 2015). The maximum CO_2 adsorption capacity of all samples ranged from 0.41 cm^3/g to 1.12 cm^3/g at a relative pressure (p/p_0) of 0.03, which decreased with increasing maturity. The maximum amount of CO_2 adsorbed by the extracted samples was higher than that of the unextracted samples at the same maturity (Fig. 4), indicating the blocking of micropores by residual oil.

The low-pressure N_2 adsorption isotherms for the investigated

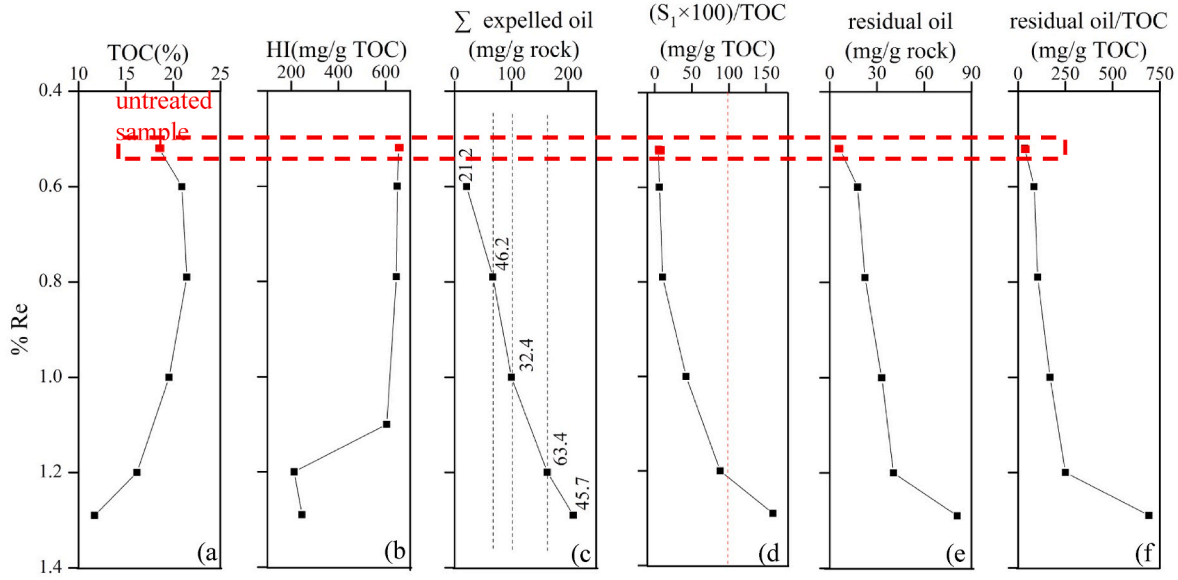

Fig. 3. Evolution characteristics of the geochemical parameters of the investigated samples. Note: In Fig. 3c, the numbers represent the amount of expelled oil at different maturities.

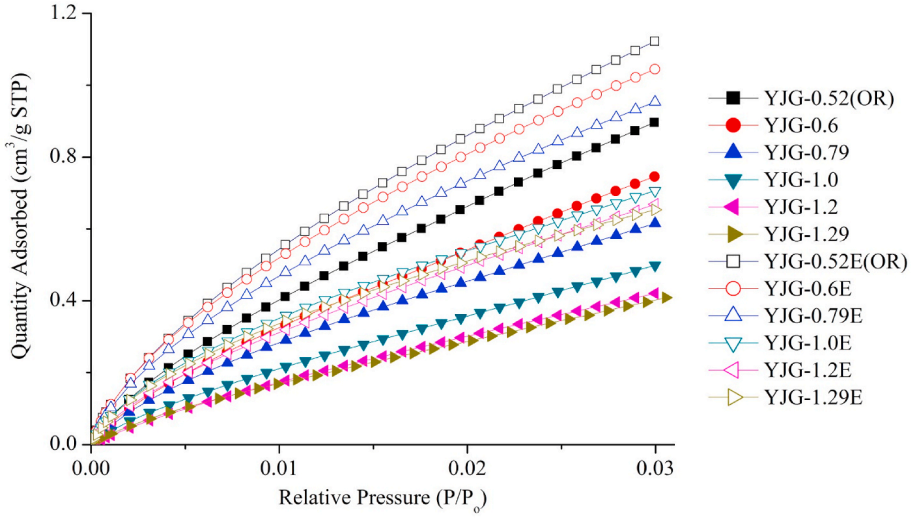

Fig. 4. CO_2 gas adsorption isotherms for the investigated samples before and after solvent extraction. Note: the number in the sample name represents the maturity (%Re); E represents extracted samples; and untreated lacustrine calcareous shale samples are represented by OR.

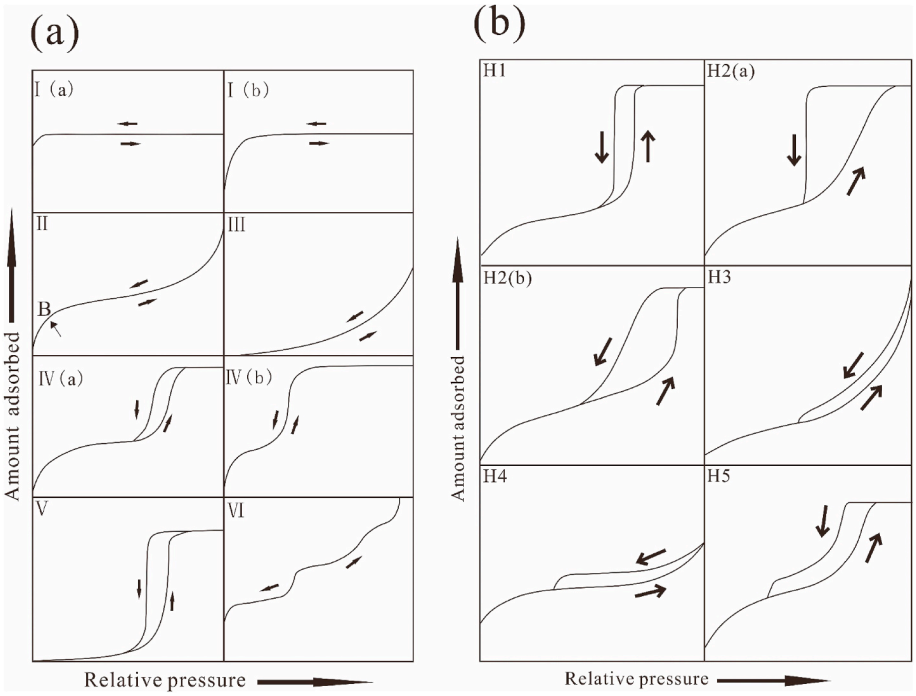

Fig. 5. Classification of (a) adsorption isotherms and (b) hysteresis loops (Thommes et al., 2015).

samples could be classed as the Type IV(a) adsorption isotherm with the Type H3 hysteresis loop based on the types of adsorption curves in the International Union of Pure and Applied Chemistry (IUPAC[17]) classification scheme (Figs. 5 and 6); this usually suggests the existence of slit-shaped pores in the aggregates of plate-like particles in shale (Thommes et al., 2015). The lower N_2 adsorption capacity at a low relative pressure ($p/p_0 < 0.01$) indicated that micropores were poorly developed in the samples. However, the N_2 adsorption capacity increased gradually with an increasing relative pressure. The absence of "forced closure" at a relative pressure of ~0.45 seemed to be caused by the instability of the hemispherical meniscus during desorption in the pores with critical diameters of ~4 nm (Groen et al., 2003). The maximum N_2 adsorption capacity of all samples ranged from 3.23 cm^3/g to 12.44 cm^3/g at a relative pressure of ~1. The maximum N_2 adsorption capacity of the unextracted samples decreased gradually with increasing maturity. However, no relationship was established between the maturity and maximum N_2 adsorption capacity of the extracted samples. The maximum amount of N_2 adsorbed by the extracted samples was higher than that of the unextracted samples at the same maturity (Fig. 6), indicating the presence of mesopores and macropores blocked by residual oil.

4.3. *vol and surface area characteristics of nanopores*

To better analyze the variation of nanopores in the lacustrine calcareous shale as a function of maturity, the nanopores were subdivided into micropores (pore diameter <2 nm), mesopores (pore diameter of 2–50 nm), and macropores (pore diameter >50 nm) (Sing et al., 1985), based on the classification of nanopores by the IUPAC.

The pore volume profile for pores of different sizes was obtained by

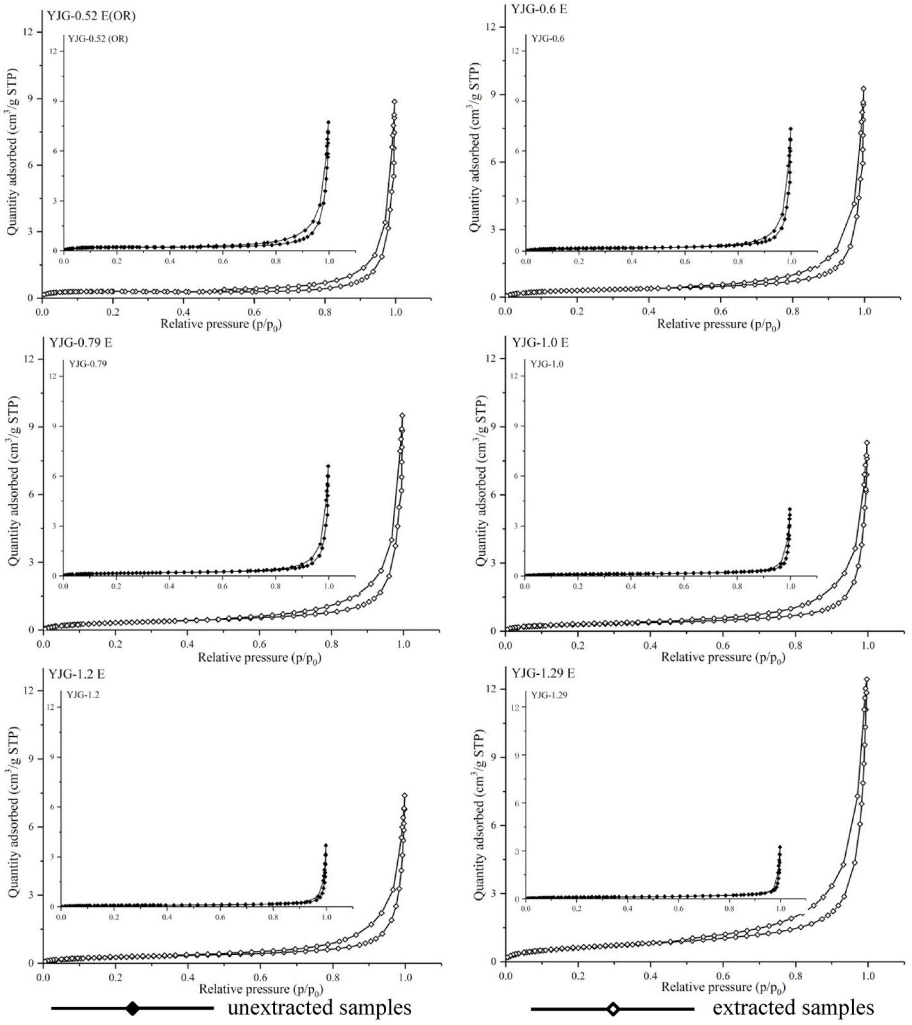

Fig. 6. N_2 gas adsorption isotherms for the investigated samples before and after solvent extraction.

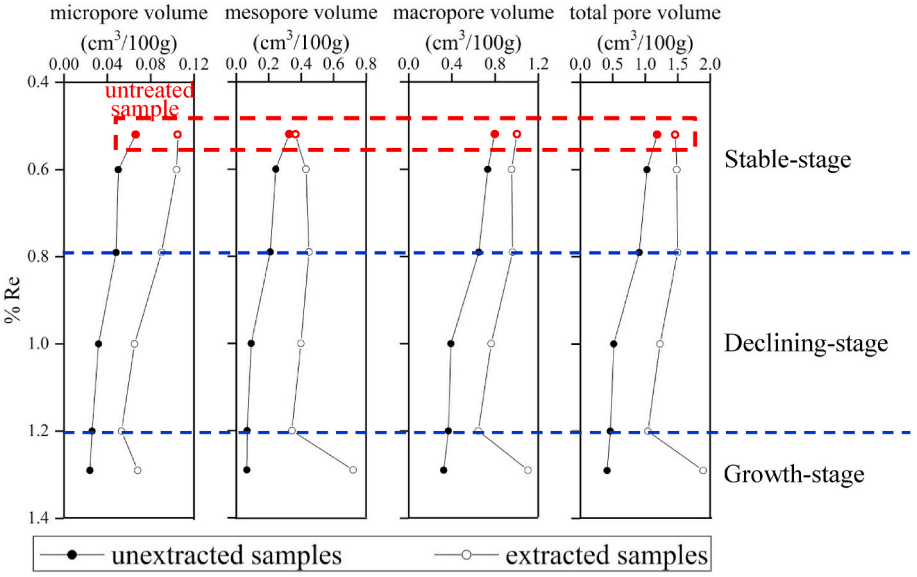

Fig. 7. Variation in the volume of nanopores of the investigated samples before and after solvent extraction.

combining the N_2 and CO_2 adsorption data (Fig. 7). The extracted samples had a noticeably greater pore volume than the unextracted samples, which corresponded with the maximum N_2 and CO_2 adsorbed. It is noteworthy that the mesopore volume, macropore volume, and total pore volume of YJG-1.29 E increased to 0.72 cm^3/g, 1.10 cm^3/g, and 1.89 cm^3/g, respectively. The values were significantly higher than those of other samples; however, the situation of the micropore volume was not evident.

The profiles of the surface area of the pores with different sizes was acquired by combining the N_2 and CO_2 adsorption data (Fig. 8). The surface area of all nanopores of the unextracted samples was seen to gradually decrease with increasing maturity. The surface area of the micropores and the total pores of the extracted samples decreased gradually with increasing maturity; however, that of the mesopores and macropores first roughly decreased, and then increased thereafter.

4.4. PSD

Here, the N_2 (1.7–300 nm, i.e., the pore size characterized by N_2 adsorption) and CO_2 (<2 nm, i.e., the pore size characterized by CO_2 adsorption) adsorption data were combined to understand the PSD in the range of 0.3–300 nm. Plots of dV/dlog(W) versus pore width (W) were used to investigate PSD, as this would help assess the partial porosity of pores considering any pore width, and help amplify the concentrations of the larger pores (Tian et al., 2013; Wang et al., 2018). The unextracted and extracted samples had similar PSDs, but the extracted samples had higher dV/dlog(W) values than the unextracted samples. The PSDs of all samples showed modes at approximately 0.5–0.8 nm, 10–108 nm, and 115–120 nm. The dV/dlog(W) values considering the pores (10–108 nm) of the extracted samples at 1.0–1.29 %Re were significantly higher than those of the unextracted samples (Fig. 9). This suggested that a large amount of residual oil was stored in mesopores and macropores at 1.0–1.29 %Re.

4.5. FE-SEM imaging and pore types

The FE-SEM images clearly showed the size, type, location, and arrangement of pores in the shale. Based on the relationship between the pores, mineral matrix, and OM, the pores could be sub-divided into inter-particle (interP[18]) pores, intraP pores, OM pores, and fractures (Loucks et al., 2012). Pores in the untreated lacustrine calcareous shale were dominated by mineral interP pores and intraP pores, while OM pores were absent (Fig. 10a). By integrating the data obtained through EDS, it could be concluded that intraP pores mainly developed in calcite and dolomite, because carbonates are chemically unstable (Chalmers et al., 2012; Loucks et al., 2012). IntraP pores were sparsely distributed with an irregular morphology; thus, their contribution to total porosity could be neglected. Additionally, slit-like pores developed in the gypsum particles as a result of distortion during burial. Moreover, rigid minerals (e.g., calcite and quartz) around gypsum help prevent further compaction to preserve the slit-like pores (Schieber, 2010). Slit-shaped interP pores occurred not only between minerals, but also between mineral particles and OM, occurring along the edge of the mineral particles and OM (Fig. 10a). The pore size considering the untreated lacustrine calcareous shale was generally at a nanometer-scale. OM pores were poorly developed in the untreated lacustrine calcareous shale, probably due to its immaturity.

The same pore types (intraP and interP pores) can be observed in pyrolyzed samples as compared to the untreated lacustrine calcareous shale (Fig. 10a, b, c). Moreover, other pore types could also be observed in the pyrolyzed samples, e.g., dissolution pores (Fig. 10c, d, e, f) and shrinkage OM pores (Fig. 10g) occurred at 0.79–1.29 %Re. The shrinkage OM pores developed between mineral particles and OM along the shale bedding, and were caused by a reduction in volume of the OM and the devolatilization of hydrocarbons (Klaver et al., 2016; Mathia et al., 2016); such pores are also found in the shale of the upper Permian Dalong Formation (Wei et al., 2018) and the Posidonia Shale, which contributed significantly to the increase in pore volume in the oil window (Mathia et al., 2016). Dissolution pores mainly appeared at 1.0–1.29 %Re, which could be harbor-like or irregular with a size of several microns. These dissolution pores with a size at a micron-scale in lacustrine calcareous shale could be one of the most distinct features as compared to the pores developed in clay-rich shale (Milliken et al., 2013).

5. Discussion

5.1. Variation in oil saturation of lacustrine calcareous shale in the oil window

Shale oil is mainly stored as adsorbed oil within and on the surface of OM pores, as free oil in micro-fractures, and as free and adsorbed oil in mineral pores (Wang et al., 2015a). The shale oil generated in shale is partially adsorbed by the shale itself; the remainder of the oil (excluding

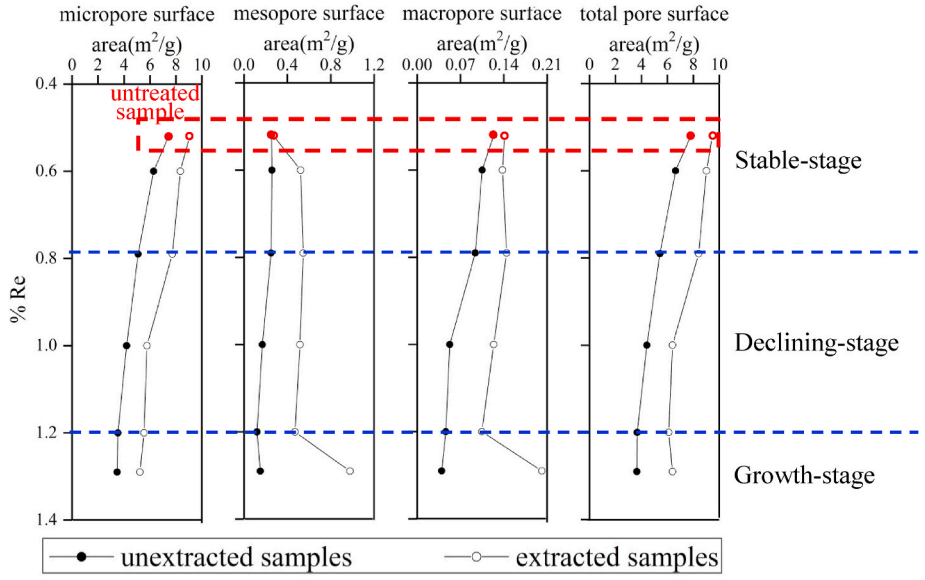

Fig. 8. Variation in the surface area of nanopores of the investigated samples before and after solvent extraction.

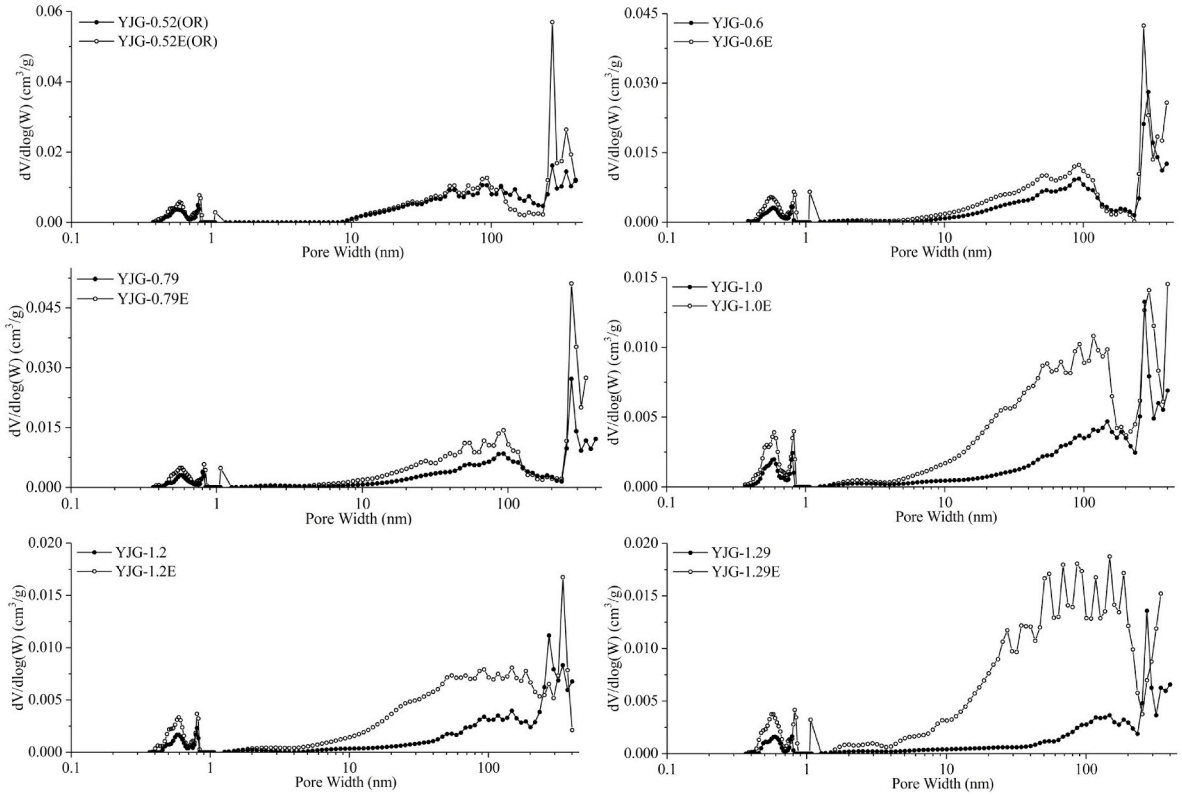

Fig. 9. Plots of dV/dlog(W) versus pore width for the investigated samples before and after solvent extraction.

the adsorbed saturated oil) could flow within the shale and is utilized in industrial exploitation. Movable shale oil is of great significance and can be evaluated by the OSI. The OSI could be obtained either by measuring the amount of chloroform bitumen "A" or by the formula "(S_1 × 100)/TOC" (Jarvie, 2012; Zhang et al., 2014).

Here, the OSI by measuring the amount of chloroform bitumen "A" was calculated by the following equation:

$$OSI = (A / D_o) / (P / D_S) \times 100 \quad (2)$$

where A is the mass percentage of chloroform bitumen "A" (%); D_o is the density of shale oil (cm^3/g); and P and D_S are the total porosity (%) and bulk density of shale (cm^3/g), respectively.

The OSI reflects the ratio of the volume of oil to the pore volume of shale; it is determined by P and A to a large extent. The total porosity and bulk density were determined by the methods described in section 3.5, while the density of shale oil was assumed to be 0.9 g/cm^3 (Liu et al., 2012a).

The value of (S_1 × 100)/TOC increased gradually with increasing maturity (Fig. 3d); additionally, this value at high maturity (1.0–1.29 %Re) was higher than that at low maturity. Generally, the variation in (S_1 × 100)/TOC was similar to that for the "residual oil/TOC" (Fig. 3d, f). The maximum increase in the OSI of the treated lacustrine calcareous shale was nearly 20% higher than that of the untreated lacustrine calcareous shale (Table 3). Our result corresponded with the increase in the OSI of the Shahejie Formation in the Dongying sag with increasing depth within a certain depth range (Zhang et al., 2014). The oil saturation of YJG-0.6 was noticeably lower than that of YJG-OR, which was probably caused by a relatively rapid increase in total porosity than by an increase in the amount of chloroform bitumen "A" in the early stage of the oil window. Subsequently, total porosity increased relatively slowly, while the amount of chloroform bitumen "A" increased relatively rapidly in the samples during a maturity range of 0.79–1.29 %Re, resulting in an increased OSI.

The OSI is considered to be an indicator for evaluating the sweet spot of shale oil when OSI >60% (Zou et al., 2015). The results suggest that a maturity range of 0.79–1.29 %Re should be targeted for shale oil exploration, as the OSI had reached 60%. Note that the total porosity of shale could be underestimated if hydrocarbon-generating seams are unevaluated by helium pycnometry, resulting in an overestimated OSI calculated using the chloroform bitumen "A" method. Nevertheless, the OSI tends to increase with increasing maturity. Moreover, Jarvie (2012) pointed out that an OSI value (S_1 × 100/TOC) above 100 was an indicator of potentially producible oil. Here, the OSI increased significantly from 88.2 to 159.6 at a maturity range of 1.2–1.29 %Re (Fig. 3d). Thus, the exploration and development of shale oil in lacustrine calcareous shale could focus on a maturity range of 1.2–1.29 %Re.

Here, the favorable maturity range (1.2–1.29 %Re) for the exploration of shale oil in lacustrine calcareous shale as determined by the OSI did not correspond with the main peak oil window (1.0–1.29 %Re) (Fig. 3). However, the sweet spot considering shale oil exploration did not exactly correspond with the main peak oil window, because shale oil generated in the late oil window had higher mobility than that generated during the early oil window. Here, the favorable maturity range, considering lacustrine calcareous shale oil exploitation, was between the peak of oil generation and the beginning of the oil cracking process (1.29% Re), which corresponded with the sweet spot for shale oil exploitation in marine calcareous shale (Zhang et al., 2017).

5.2. *Pore evolution of lacustrine calcareous shale during kerogen maturation*

Pore evolution was the core aspect of the shale reservoir assessment. The shale had a complex pore network controlled by various factors. For example, the mineral composition of the shale played a fundamental role in the development of mineral interP and intraP pores, whereas the formation of OM pores was governed by maturity, and the type and content of OM (Milliken et al., 2013; Chen and Xiao, 2014; Liu et al., 2019a). The volume of OM would decrease with increasing maturity due

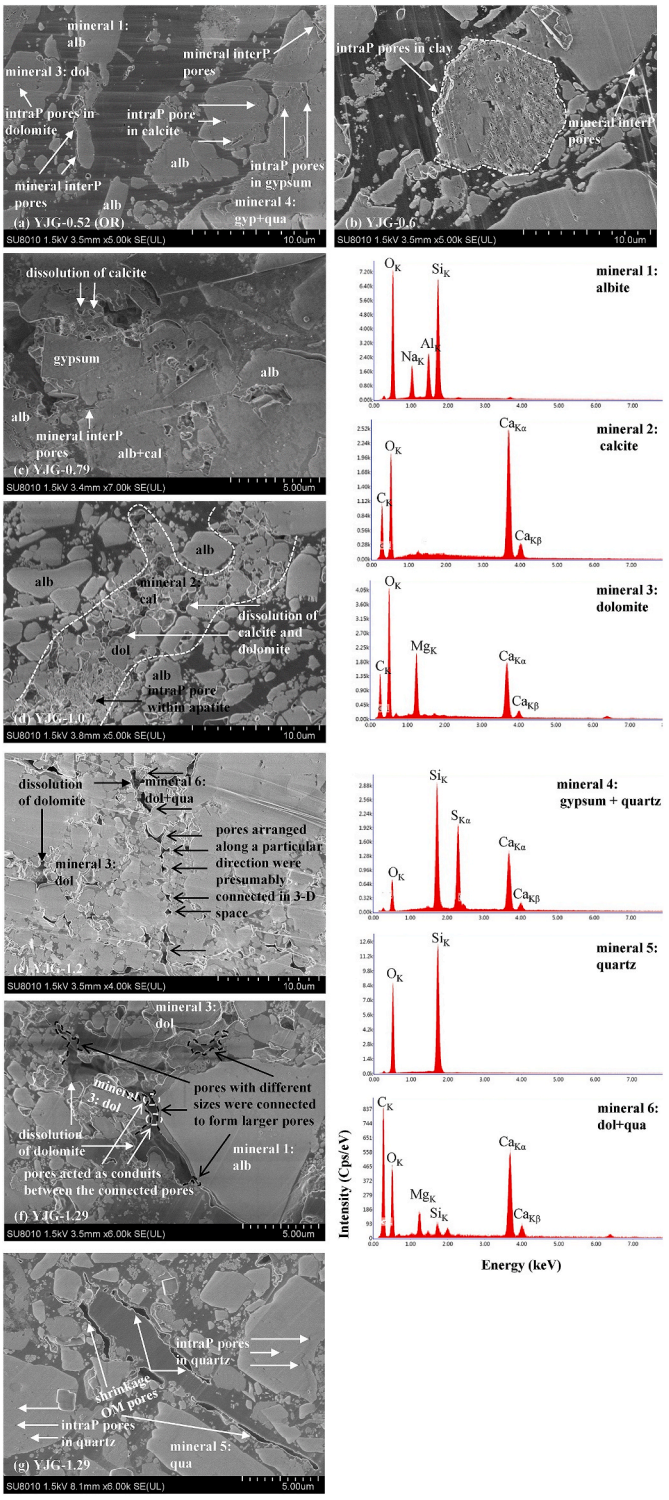

Fig. 10. FE-SEM images of the samples at different maturities, and integration of Energy Dispersive X-ray Spectroscopy (EDS) data. Note: qua: quartz; alb: albite; cal: calcite; dol: dolomite; and gyp: gypsum.

to hydrocarbon generation and expulsion.

Additionally, the interaction between organic acids and soluble minerals leads to the formation of dissolution pores (Seewald, 2003; Luan et al., 2016; Nie et al., 2019). Moreover, numerous studies have demonstrated that maturity is a key factor in the development and evolution of nanopores in shale (Chen and Xiao, 2014; Löhr et al., 2015). Here, a series of samples with increased maturity were obtained in the oil window. Therefore, it was reasonable to study the influence of maturity on the pore evolution of lacustrine calcareous shale.

Table 3
Parameters of total porosity and oil saturation of the investigated samples.

Sample name	Bulk density (cm^3/g)	Grain density (cm^3/g)	Total porosity (%)	Chloroform bitumen "A" (%)	Oil saturation (%)
YJG-OR	1.927	1.974	2.38	0.65	58.26
YJG-0.6	1.905	2.059	7.48	1.77	50.08
YJG-0.79	1.923	2.090	7.99	2.24	59.78
YJG-1.0	2.011	2.234	9.98	3.30	73.94
YJG-1.2	2.065	2.346	11.98	4.05	77.55
YJG-1.29	1.967	2.554	22.98	8.09	76.93

5.2.1. *Nanopore evolution*

Both the volume and surface area of the micropores of the pyrolyzed samples before and after solvent extraction were lower than that of the untreated lacustrine calcareous shale (Figs. 7 and 8); this could be explained by the merging of some micropores into larger pores during pyrolysis. The changes in the volume and surface area of the mesopores and macropores of the extracted samples could be roughly divided into three stages: stable-stage (at 0.52–0.79 %Re), declining-stage (at 0.79–1.2 %Re), and growth-stage (at 1.2–1.29 %Re) (Figs. 7 and 8). The change in pore type in the stable-stage was insignificant (Fig. 10a, b, c), although dissolution pores occurred at 0.79 %Re (Fig. 10c). Moreover, the pore size had no noticeable change during the stable-stage, as indicated by the relatively constant PSDs of the three samples (YJG-0.52 E, YJG-0.6 E, and YJG-0.79 E) (Fig. 9). The decreasing mesopore volume during the declining-stage could be attributed to the clogging of pores by generated bitumen (Valenza et al., 2013; Liu et al., 2019a). This was also supported by the fact that the volume and surface area of the mesopores and macropores of the pyrolyzed samples after solvent extraction was higher than that before solvent extraction (Figs. 7 and 8). Additionally, it could be speculated that the residual oil and bitumen were mainly stored in the mesopores and macropores, which was indicated by the significant difference between the PSDs of YJG-1.0 and YJG-1.2; and YJG-1.0 E and YJG-1.2 E; this was also in accordance with a previous study (Li et al., 2015a). However, considering the extracted samples, their pore volume and surface area in the declining-stage were lower than that in the stable-stage. The intense compaction led to the densification of the shale in the declining-stage, resulting in a decrease in the nanopores. This interpretation is consistent with the fact that the density of the pyrolyzed samples in the declining-stage was higher than that in the stable-stage (Table 3). Okiongbo et al. (2005) found that a noticeable increase in density did not occur before 0.8 %Ro for kerogen in the Kimmeridge Clay Formation.

The growth-stage occurred at the end of the oil window with significant hydrocarbon generation and expulsion (Fig. 3c, e). The amount of expelled oil at 1.29 %Re was lower than that at 1.2 %Re (Fig. 3c), probably indicating the beginning of the cracking of oil to gas at 1.29 % Re. Therefore, the characteristics of hydrocarbon generation and expulsion at a maturity of 1.29 %Re could signify the beginning of the gas window. Further thermal degradation of OM at 1.29 %Re could lead to the formation of OM pores, resulting in a rapid increase in the pore volume and surface area for lacustrine calcareous shale. The nanopore development of shale under pyrolysis and under geological conditions illustrated that secondary OM pores formed at the end of the oil window or in the gas window (Curtis et al., 2012; Chen and Xiao, 2014; Pommer and Milliken, 2015).

To be different, no OM pores were observed in the unextracted samples at 1.29 %Re (Fig. 10f and g); moreover, the pore volume of the extracted samples at 1.29 %Re increased significantly, relative to that at 1.2 %Re (Fig. 7). To address this problem, the extracted samples were analyzed through FE-SEM at 1.2 %Re and 1.29 %Re. No OM pores were

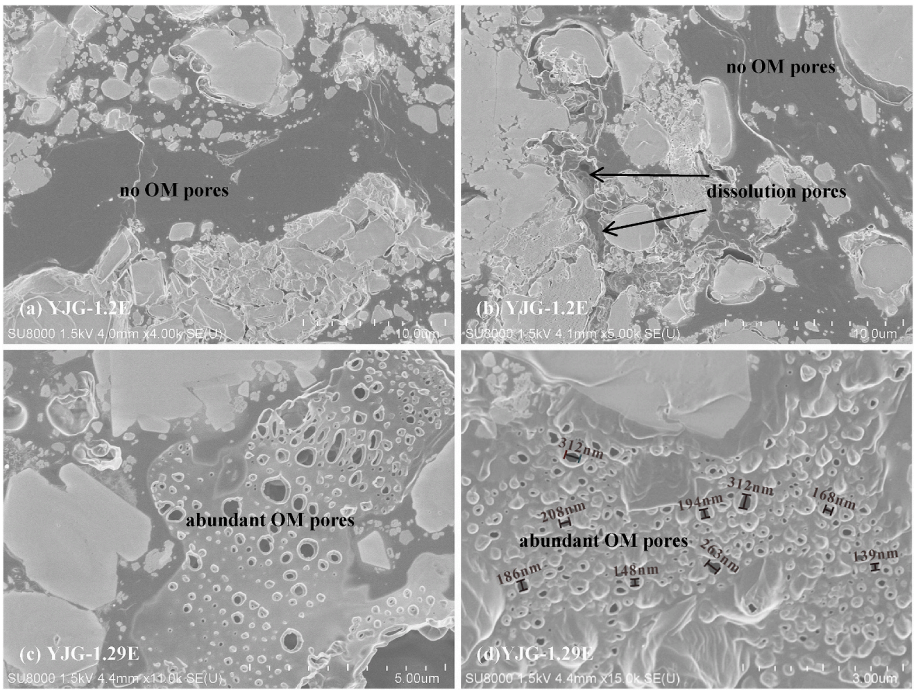

Fig. 11. Comparison of the development of OM pores in the extracted samples between 1.29 %Re and 1.2 %Re. Note: In Fig. 11d, the numbers represent the pore diameter of the OM pores.

observed in the extracted samples at 1.2 %Re (Fig. 11a and b), whereas abundant OM pores of size <300 nm (detection limit for low-pressure gas adsorption) were observed at 1.29 %Re (Fig. 11c and d). This clearly demonstrated that secondary OM pores were generated and blocked by residual oil at the growth-stage. Moreover, secondary OM pores did not appear until 1.29 %Re, indicating that thermal maturity was the key factor controlling the development of OM pores.

5.2.2. Dissolution pores

Dissolution pores are important in carbonate-bearing shale reservoirs. They can develop within grains and at grain edges, and provide space for shale oil (Nie et al., 2019; Zhang et al., 2019; Wang and Wang, 2020). The unstable minerals including carbonates (calcite and dolomite), feldspar, and quartz could dissolve to form dissolution pores in the oil window (Loucks et al., 2012; Milliken et al., 2013; Nie et al., 2019; Zhang et al., 2019). Organic acids were thought to be the primary fluids involved in the dissolution process in shale that was accompanied by the decarboxylation of kerogen and the expulsion of hydrocarbon-bearing fluids (Schieber, 2010). The carbonate content of the lacustrine calcareous shale was 29.6%; moreover, the TOC content kept dropping at 0.79–1.29 %Re, while large amounts of oil were expelled (Fig. 3a, c). This was in correspondence with the fact that dissolution pores developed and were mainly distributed around and within the carbonate minerals based on the FE-SEM and EDS at 0.79–1.29 %Re (Fig. 10c, d, e, f). Moreover, the dissolution pores had a harbor-like shape and a large variation in pore diameter from nanometer-scale to micron-scale (Fig. 10c, d, e, f). Subsequently, the dissolution pores merged to form larger pores, while the smaller pores acted as conduits between the connected pores (Fig. 10f). Note that dissolution pores arranged along a particular direction in a 2-D image were presumably connected in 3-D space (Fig. 10e). Dissolution pores at a micron-scale were widely distributed at 1.0–1.29 %Re (Fig. 10d, e, f), which could improve the storage capacity of a lacustrine calcareous shale reservoir.

Furthermore, slit-shaped pores with lengths extending to several microns developed along the margin of OM, which were called as shrinkage OM pores (Fig. 10g); such pores were caused by a reduction in the volume of OM due to thermal degradation. Consequently, dissolution pores and shrinkage OM pores together largely contributed to improved reservoir performance (Nie et al., 2019); this corresponded with the continuously increasing total porosity of the pyrolyzed samples (Table 3).

In summary, the reduction of pores in the lacustrine calcareous shale resulted from the blocking of nanopores by residual oil and intense compaction. Moreover, the shale oil reservoir of the lacustrine calcareous shale was enhanced by the formation of dissolution pores caused by the interaction between carbonate minerals and organic acids, and the development of OM pores. The OM pores formed due to the thermal degradation of OM accompanied by hydrocarbon generation and expulsion. The maturity stage (1.2–1.29 %Re) is favorable considering shale oil exploration in lacustrine calcareous formations, based on the development of dissolution pores, shrinkage OM pores, and a high OSI. The evolution and development of pores in the lacustrine calcareous shale were controlled by various factors, viz., OM maturity, hydrocarbon generation and expulsion, and organic-inorganic interactions.

6. Conclusions

Here, lacustrine calcareous shale of the middle Permian Lucaogou Formation in the Santanghu Basin was pyrolyzed in a semi-closed system for thermal simulation to study the hydrocarbon generation and expulsion, oil bearing capacity, and the evolution of pores with increasing maturity. The main findings were as follows:

(1) The total amount of expelled and residual oil increased gradually with increasing maturity, reaching maximum values of 208.90 mg/g rock and 80.93 mg/g rock, respectively. Accordingly, the OSI calculated based on the residual oil content (Eq. (2)) increased with increasing maturity at 0.6–1.29 %Re, while that calculated using the formula "$S_1 \times 100/TOC$" increased from 88.2 at 1.2 %Re to 159.6 at 1.29 %Re.
(2) The changes in the volume and surface area of the mesopores and macropores of the extracted shale samples could be grouped into three stages: stable-stage (at 0.52–0.79 %Re), declining-stage (at

0.79–1.2 %Re), and growth-stage (at 1.2–1.29 %Re). The pore type and PSDs showed no noticeable changes during the stable-stage. The blocking of pores by generated oil and intense compaction caused a decrease in the volume of mesopores and macropores during the declining-stage. Abundant OM pores formed due to significant hydrocarbon generation and expulsion in the lacustrine calcareous shale at 1.29 %Re. Thermal maturity was the key factor controlling the development of OM pores.

(3) Dissolution pores and shrinkage OM pores with sizes at a micron-scale, helped increased the total porosity and improve the storage capacity of the lacustrine calcareous shale oil reservoir at 1.0–1.29 %Re. A maturity range of 1.2–1.29 %Re is favorable for shale oil exploration in lacustrine calcareous shale, due to the widely developed dissolution pores, shrinkage OM pores, and a high OSI ($S_1 \times 100/TOC$).

Declaration of competing interest

The authors declare that they have no known competing financial interests or personal relationships that could have appeared to influence the work reported in this paper.

Acknowledgements

This work was supported by the Strategic Priority Research Program of the Chinese Academy of Sciences , China [XDA14010102]; the GIG-135 Shale Gas Project, China [135TP201602]; the National Natural Science Foundation of China [41602130, 41673045, 41930426]; and the China Postdoctoral Science Foundation [2019M653713]. The authors thanked two anonymous reviewers for their comments, which largely improved the manuscript. This is contribution No. IS-2957 from GIGCAS.

Appendix A. Supplementary data

Supplementary data to this article can be found online at https://doi.org/10.1016/j.petrol.2020.108230.

References

Chalmers, G.R., Bustin, R.M., Power, I.M., 2012. Characterization of gas shale pore systems by porosimetry, pycnometry, surface area, and field emission scanning electron microscopy/transmission electron microscopy image analyses: examples from the Barnett, Woodford, Haynesville, Marcellus, and Doig units. Am. Assoc. Petrol. Geol. Bull. 96 (6), 1099–1119. https://doi.org/10.1306/10171111052.

Chen, J., Xiao, X., 2014. Evolution of nanoporosity in organic-rich shales during thermal maturation. Fuel 129, 173–181. https://doi.org/10.1016/j.fuel.2014.03.058.

Clarkson, C.R., Jensen, J.L., Pedersen, P.K., et al., 2012. Innovative methods for flow-unit and pore-structure analyses in a tight siltstone and shale gas reservoir. Am. Assoc. Petrol. Geol. Bull. 96 (2), 355–374. https://doi.org/10.1306/05181110171.

Curtis, M.E., Cardott, B.J., Sondergeld, C.H., et al., 2012. Development of organic porosity in the Woodford Shale with increasing thermal maturity. Int. J. Coal Geol. 103, 26–31. https://doi.org/10.1016/j.coal.2012.08.004.

Dombrowski, R.J., Hyduke, D.R., Lastoskie, C.M., 2000. Pore size analysis of activated carbons from argon and nitrogen porosimetry using density functional theory. Langmuir 16 (11), 5041–5050. https://doi.org/10.1021/la990827a.

Du, J., Cheng, B., Liao, Z., 2014. Geochemical characterization of gaseous pyrolysates from a Permian kerogen of Santanghu Basin. Geochimica 43 (5), 510–517.

Ehrenberg, S.N., Nadeau, P.H., 2005. Sandstone vs. carbonate petroleum reservoirs: a global perspective on porosity-depth and porosity-permeability relationships. Am. Assoc. Petrol. Geol. Bull. 89 (4), 435–445. https://doi.org/10.1306/11230404071.

Fishman, N.S., Hackley, P.C., Lowers, H.A., et al., 2012. The nature of porosity in organic-rich mudstones of the upper jurassic Kimmeridge Clay Formation, North sea, offshore United Kingdom. Int. J. Coal Geol. 103, 32–50. https://doi.org/10.1016/j.coal.2012.07.012.

Fu, J., Liu, D., Sheng, G., 1990. Geochemistry of Coal-Generated Hydrocarbons. Geological Publishing House, Beijing, pp. 348–355.

Groen, J.C., Peffer, L.A.A., Pérez-Ramírez, J., 2003. Pore size determination in modified micro- and mesoporous materials. Pitfalls and limitations in gas adsorption data analysis. Microporous Mesoporous Mater. 60 (1–3), 1–17. https://doi.org/10.1016/s1387-1811(03)00339-1.

Hackley, P.C., Fishman, N., Wu, T., et al., 2016. Organic petrology and geochemistry of mudrocks from the lacustrine Lucaogou Formation, Santanghu Basin, northwest China: application to lake basin evolution. Int. J. Coal Geol. 168, 20–34. https://doi.org/10.1016/j.coal.2016.05.011.

Huang, Z., Guo, B., Liu, B., et al., 2012. The reservoir space characteristics and origins of Lucaogou Formation source rock oil in the Malang Sag. Acta Sedimentol. Sin. 30 (6), 1115–1122.

Jarvie, D.M., 2012. Shale resource systems for oil and gas: part 2—shale-oil resource systems. AAPG Mem 97, 89–119.

Klaver, J., Desbois, G., Littke, R., et al., 2016. BIB-SEM pore characterization of mature and post mature Posidonia Shale samples from the Hils area, Germany. Int. J. Coal Geol. 158, 78–89. https://doi.org/10.1016/j.coal.2016.03.003.

Lewan, M.D., 1985. Evaluation of petroleum generation by hydrous phyrolysis experimentation. Phil. Trans. Roy. Soc. Lond. 315 (1531), 123–134. https://doi.org/10.1098/rsta.1985.0033.

Lewan, M.D., Roy, S., 2011. Role of water in hydrocarbon generation from Type-I kerogen in Mahogany oil shale of the Green River Formation. Org. Geochem. 42 (1), 31–41. https://doi.org/10.1016/j.orggeochem.2010.10.004.

Li, J., Ma, Y., Huang, K., et al., 2018. Quantitative characterization of organic acid generation, decarboxylation, and dissolution in a shale reservoir and the corresponding applications—a case study of the Bohai Bay Basin. Fuel 214, 538–545. https://doi.org/10.1016/j.fuel.2017.11.034.

Li, J., Shi, Y., Huang, Z., et al., 2015a. Pore characteristics of continental shale and its impact on storage of shale oil in northern Songliao Basin. Journal of China University of Petroleum (Edition of Natural Science) 39 (4), 27–34. https://doi.org/10.3969/j.issn.1673-5005.2015.04.004.

Li, X., Ma, Q., Liang, H., et al., 2015b. Geological characteristics and exploration potential of diamictite tight oil in the second Member of the Permian Lucaogou Formation, Santanghu Basin, NW China. Petrol. Explor. Dev. 42 (6), 833–843. https://doi.org/10.1016/s1876-3804(15)30080-x.

Li, Z., Zou, Y., Xu, X., et al., 2016. Adsorption of mudstone source rock for shale oil – experiments, model and a case study. Org. Geochem. 92, 55–62. https://doi.org/10.1016/j.orggeochem.2015.12.009.

Liang, S., Huang, Z., Liu, B., et al., 2012. Formation mechanism and enrichment conditions of Lucaogou Formation shale oil from Malang sag, Santanghu Basin. Acta Petrol. Sin. 33 (4), 588–594.

Liu, B., Bechtel, A., Sachsenhofer, R.F., et al., 2017. Depositional environment of oil shale within the second member of permian Lucaogou Formation in the Santanghu Basin, northwest China. Int. J. Coal Geol. 175, 10–25. https://doi.org/10.1016/j.coal.2017.03.011.

Liu, B., Lv, Y., Meng, Y., et al., 2015. Petrologic characteristics and genetic model of lacustrine lamellar fine-grained rock and its significance for shale oil exploration: a case study of Permian Lucaogou Formation in Malang sag, Santanghu Basin, NW China. Petrol. Explor. Dev. 42 (5), 656–666. https://doi.org/10.1016/s1876-3804(15)30060-4.

Liu, B., Lv, Y., Zhao, R., et al., 2012a. Formation overpressure and shale oil enrichment in the shale system of Lucaogou Formation, Malang sag, Santanghu Basin, NW China. Petrol. Explor. Dev. 39 (6), 744–750. https://doi.org/10.1016/s1876-3804(12)60099-8.

Liu, D., Li, H., Zhang, C., et al., 2019a. Experimental investigation of pore development of the Chang 7 member shale in the Ordos basin under semi-closed high-pressure pyrolysis. Mar. Petrol. Geol. 99, 17–26. https://doi.org/10.1016/j.marpetgeo.2018.08.014.

Liu, G., Zhai, G., Huang, Z., et al., 2019b. The effect of tuffaceous material on characteristics of different lithofacies: a case study on Lucaogou Formation fine-grained sedimentary rocks in Santanghu Basin. J. Petrol. Sci. Eng. 179, 355–377. https://doi.org/10.1016/j.petrol.2019.04.072.

Liu, Y., Jiao, X., Li, H., et al., 2012b. Primary dolostone formation related to mantle-originated exhalative hydrothermal activities, Permian Yuejingou section, Santanghu area, Xinjiang, NW China. Sci. China Earth Sci. 55 (2), 183–192. https://doi.org/10.1007/s11430-011-4356-1.

Löhr, S.C., Baruch, E.T., Hall, P.A., et al., 2015. Is organic pore development in gas shales influenced by the primary porosity and structure of thermally immature organic matter? Org. Geochem. 87, 119–132. https://doi.org/10.1016/j.orggeochem.2015.07.010.

Loucks, R.G., Reed, R.M., Ruppel, S.C., et al., 2009. Morphology, genesis, and distribution of nanometer-scale pores in siliceous mudstones of the mississippian barnett shale. J. Sediment. Res. 79 (12), 848–861. https://doi.org/10.2110/jsr.2009.092.

Loucks, R.G., Reed, R.M., Ruppel, S.C., et al., 2012. Spectrum of pore types and networks in mudrocks and a descriptive classification for matrix-related mudrock pores. Am. Assoc. Petrol. Geol. Bull. 96 (6), 1071–1098. https://doi.org/10.1306/08171111061.

Luan, G., Dong, C., Ma, C., et al., 2016. Pyrolysis simulation experiment study on diagenesis and evolution of organic-rich shale. Acta Sedimentol. Sin. 34 (6), 1208–1216.

Ma, J., Huang, Z., Li, T., 2019. Mechanism of hydrocarbon accumulation and enrichment of tuffaceous tight oil with separate reservoir and source rock: a case study of tuff reservoir from the Permian Tiaohu Formation in the Santanghu Basin, northwest China. Am. Assoc. Petrol. Geol. Bull. 103 (2), 345–367. https://doi.org/10.1306/07031817108.

Mathia, E.J., Bowen, L., Thomas, K.M., et al., 2016. Evolution of porosity and pore types in organic-rich, calcareous, Lower Toarcian Posidonia Shale. Mar. Petrol. Geol. 75, 117–139. https://doi.org/10.1016/j.marpetgeo.2016.04.009.

Milliken, K.L., Rudnicki, M., Awwiller, D.N., et al., 2013. Organic matter–hosted pore system, Marcellus Formation (Devonian), Pennsylvania. Am. Assoc. Petrol. Geol. Bull. 97 (2), 177–200. https://doi.org/10.1306/07231212048.

Nie, H., Sun, C., Liu, G., et al., 2019. Dissolution pore types of the wufeng formation and the longmaxi formation in the sichuan basin, south China: implications for shale gas enrichment. Mar. Petrol. Geol. 101, 243–251. https://doi.org/10.1016/j.marpetgeo.2018.11.042.

Okiongbo, K.S., Aplin, A.C., Larter, S.R., 2005. Changes in type II kerogen density as a function of maturity: evidence from the Kimmeridge Clay Formation. Energy Fuel. 19 (6), 2495–2499. https://doi.org/10.1021/ef050194+.

Pommer, M., Milliken, K., 2015. Pore types and pore-size distributions across thermal maturity, Eagle Ford Formation, southern Texas. Am. Assoc. Petrol. Geol. Bull. 99 (9), 1713–1744. https://doi.org/10.1306/03051514151.

Ross, D.J.K., Bustin, R.M., 2007. Shale gas potential of the lower jurassic gordondale member, northeastern British columbia, Canada. Bull. Can. Petrol. Geol. 55 (1), 51–75. https://doi.org/10.2113/gscpgbull.55.1.51.

Ross, D.J.K., Bustin, R.M., 2009. The importance of shale composition and pore structure upon gas storage potential of shale gas reservoirs. Mar. Petrol. Geol. 26 (6), 916–927. https://doi.org/10.1016/j.marpetgeo.2008.06.004.

Schieber, J., 2010. Common themes in the formation and preservation of intrinsic porosity in shale and mudstones-illustrated with examples across the Phanerozoic. SPE Unconventional Gas Conference 428. https://doi.org/10.2118/132370-MS.

Seewald, J.S., 2003. Organic–inorganic interactions in petroleum-producing sedimentary basins. Nature 426 (6964), 327–333. https://doi.org/10.1038/nature02132.

Sing, K.S.W., 1985. Reporting physisorption data for gas/solid systems with special reference to the determination of surface area and porosity (Recommendations 1984). Pure Appl. Chem. 57 (4), 603–619. https://doi.org/10.1351/pac198557040603.

Sweeney, J.J., Burnham, A.K., 1990. Evaluation of a simple model of vitrinite reflectance based on Chemical kinetics. Am. Assoc. Petrol. Geol. Bull. 74 (10), 1559–1570. https://doi.org/10.1306/0c9b251f-1710-11d7-8645000102c1865d.

Thommes, M., Kaneko, K., Neimark, A.V., et al., 2015. Physisorption of gases, with special reference to the evaluation of surface area and pore size distribution (IUPAC Technical Report). Pure Appl. Chem. 87 (9–10), 1051–1069. https://doi.org/10.1515/pac-2014-1117.

Tian, H., Pan, L., Xiao, X., et al., 2013. A preliminary study on the pore characterization of Lower Silurian black shales in the Chuandong Thrust Fold Belt, southwestern China using low pressure N_2 adsorption and FE-SEM methods. Mar. Petrol. Geol. 48, 8–19. https://doi.org/10.1016/j.marpetgeo.2013.07.008.

Valenza, J.J., Drenzek, N., Marques, F., et al., 2013. Geochemical controls on shale microstructure. Geology 41 (5), 611–614. https://doi.org/10.1130/g33639.1.

Wang, Q., Lu, H., Wang, T., et al., 2018. Pore characterization of Lower Silurian shale gas reservoirs in the Middle Yangtze region, central China. Mar. Petrol. Geol. 89, 14–26. https://doi.org/10.1016/j.marpetgeo.2016.12.015.

Wang, Q., Wang, T., 2020. Detection of dissolution pores in the marginally mature calcareous Lucaogou shale: new insights in nanopore development in terrestrial shale oil reservoirs. Acta Geol. Sin-Engl. https://doi.org/10.1111/1755-6724.14417.

Wang, Q., Wang, T., Liu, W., et al., 2019. Relationships among composition, porosity and permeability of longmaxi shale reservoir in the weiyuan block, sichuan basin, China. Mar. Petrol. Geol. 102, 33–47. https://doi.org/10.1016/j.marpetgeo.2018.12.026.

Wang, W., Zheng, M., Wang, M., et al., 2015a. The discussion of the evaluation method of shale oil movable resources amount and Palaeogene Shahejie Formation application effect in the northern of Dongpu Depression. Natural Gas Geoscience 26, 771–781.

Wang, X., Zhang, L., Jiang, C., et al., 2015b. Hydrocarbon storage space within lacustrine gas shale of the triassic yanchang formation, Ordos Basin, China. Interpretation 3 (2). https://doi.org/10.1190/int-2014-0125.1. SJ15–SJ23.

Wei, M., Xiong, Y., Zhang, L., et al., 2016a. The effect of sample particle size on the determination of pore structure parameters in shales. Int. J. Coal Geol. 163, 177–185. https://doi.org/10.1016/j.coal.2016.07.013.

Wei, M., Zhang, L., Xiong, Y., et al., 2016b. Nanopore structure characterization for organic-rich shale using the non-local-density functional theory by a combination of N_2 and CO_2 adsorption. Microporous Mesoporous Mater. 227, 88–94. https://doi.org/10.1016/j.micromeso.2016.02.050.

Wei, Z., Wang, Y., Wang, G., et al., 2018. Pore characterization of organic-rich late permian da-long Formation shale in the sichuan basin, southwestern China. Fuel 211, 507–516. https://doi.org/10.1016/j.fuel.2017.09.068.

Yang, Z., Chen, X., Li, Q., et al., 2020. Permian sedimentary tuff tight reservoirs in the Santanghu Basin, NW China. Mar. Petrol. Geol. 119, 104447. https://doi.org/10.1016/j.marpetgeo.2020.104447.

Zhang, J., Lin, L., Li, Y., et al., 2012. Classification and evaluation of shale oil. Earth Sci. Front. 19 (5), 322–331.

Zhang, L., Bao, Y., Li, J., et al., 2014. Movability of lacustrine shale oil: a case study of dongying sag, jiyang depression, Bohai Bay Basin. Petrol. Explor. Dev. 41 (6), 703–711. https://doi.org/10.1016/s1876-3804(14)60084-7.

Zhang, L., Chen, Z., Li, Z., et al., 2019. Structural features and genesis of microscopic pores in lacustrine shale in an oil window: a case study of the Dongying depression. Am. Assoc. Petrol. Geol. Bull. 103 (8), 1889–1924. https://doi.org/10.1306/1218181522717084.

Zhang, S., Liu, C., Liang, H., et al., 2018. Paleoenvironmental conditions, organic matter accumulation, and unconventional hydrocarbon potential for the Permian Lucaogou Formation organic-rich rocks in Santanghu Basin, NW China. Int. J. Coal Geol. 185, 44–60. https://doi.org/10.1016/j.coal.2017.11.012.

Zhang, T., Sun, X., Milliken, K.L., et al., 2017. Empirical relationship between gas composition and thermal maturity in Eagle Ford Shale, south Texas. Am. Assoc. Petrol. Geol. Bull. 101 (8), 1277–1307. https://doi.org/10.1306/09221615209.

Zheng, Y., Liao, Y., Wang, Y., et al., 2018. Organic geochemical characteristics, mineralogy, petrophysical properties, and shale gas prospects of the Wufeng–Longmaxi shales in Sanquan Town of the Nanchuan District, Chongqing. Am. Assoc. Petrol. Geol. Bull. 102 (11), 2239–2265. https://doi.org/10.1306/04241817065.

Zou, C., Yang, Z., Cui, J., et al., 2013. Formation mechanism, geological characteristics and development strategy of nonmarine shale oil in China. Petrol. Explor. Dev. 40 (1), 15–27. https://doi.org/10.1016/s1876-3804(13)60002-6.

Zou, C.N., Zhu, R.K., Bai, B., et al., 2015. Significance, geologic characteristics, resource potential and future challenges of tight oil and shale oil. Bull. China Soc. Mineral Petrol. Geochem. 34 (1), 3–17. https://doi.org/10.3969/j.issn.1007-2802.2015.01.001.